

Thesis

Fabrizio Chinu

October 2023

Chapter 1

High-energy nuclear physics

1.1 Quantum Chromodynamics

In the mid-20th century, the realm of particle physics underwent a transformative phase, marked by the discovery of a seemingly endless variety of subatomic particles. This era witnessed the unveiling of numerous mesons and baryons, which left physicists with the necessity of developing a framework that could describe the behaviour of these particles and their interactions. This led to the development of the static quark model, which emerged in the 1960s as a groundbreaking conceptual framework to categorize the various observed particles. Developed independently by Murray Gell-Mann[1] and George Zweig[2, 3], this model postulated the existence of fundamental constituents called quarks, which, in order to reflect the experimental findings, had to be fermions (to describe baryons with spin 1/2 and 3/2) with fractional electric charge. The quark model beautifully explained the organization of hadrons in terms of three quarks (u , d , and s), leading to the development of a more structured and coherent classification of particles.

Despite the phenomenological success of the static quark model, it had two problems: it introduced particles with fractional charge, which had never been observed before, and, most importantly, it gave rise to a violation of the Fermi-Dirac statistics. The Δ^{++} , Δ^- , and Ω^- baryons, in fact, have symmetric orbital, spin and flavour wavefunctions, which defied the Pauli exclusion principle that should have implied antisymmetric wavefunctions for these particles.

To resolve these inconsistencies, a new degree of freedom, the *colour*, was introduced. Hadrons wavefunctions were assumed to be totally antisymmetric in colour quantum numbers, effectively implementing the Pauli exclusion principle.

The simplest model of colour would be to assign quarks to the fundamental representation of a global $SU(3)$ symmetry. Each quark now carries a colour index: q_i , where $i = 1, 2, 3$, and transforms under the fundamental (3) representation of $SU(3)$, while antiquarks, \bar{q}_i , transform in the $\bar{3}$ representation. Introducing the totally antisymmetric tensor ε^{ijk} , possible compositions of quarks

that give rise to colour singlets are

$$\bar{q}^i q_i, \quad \varepsilon^{ijk} q_i q_j q_k, \quad \varepsilon^{ijk} \bar{q}_i \bar{q}_j \bar{q}_k,$$

which are the quarks compositions of mesons, baryons, and antibaryons, respectively.

One of the tests supporting the existence of colour and fractional electric charge came in the form of the ratio R , of the e^+e^- total hadronic cross-section to the cross-section of a pair of muons produced from the same annihilation process. The virtual photon emitted in the annihilation can produce all electrically charged pairs of particles and antiparticles, as shown in Fig. 1.1.

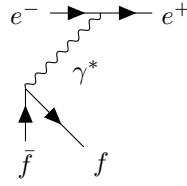


Figure 1.1: e^+e^- annihilation to a pair of fermions

The ratio R is given by:

$$R = \frac{\sigma(e^+e^- \rightarrow \text{hadrons})}{\sigma(e^+e^- \rightarrow \mu^+\mu^-)} = N_c \sum_f Q_f^2,$$

where N_c represents the number of existing colours and Q_f is the electric charge of the quark flavour f . Notably, this ratio is dependent on the energy of the center-of-mass system and encompasses all possible quark flavors that can be produced by the virtual photon at that specific energy level. The experimental data for R (shown in Fig. 1.2) exhibited a remarkable agreement with the predictions of the three-color model, thereby providing compelling evidence for the existence of color and fractional electric charge of quarks.

The final step that propelled the development of QCD as a comprehensive theory of the strong force was the insight into the mechanism that ensured all hadron wavefunctions to be color singlets. This emerged from the discovery of asymptotic freedom, a phenomenon observed in deep-inelastic scattering experiments. Non-Abelian gauge theories, often referred to as Yang-Mills theories, were identified as having this unique characteristic. This realization led to the formulation of QCD by elevating the global color $SU(3)$ symmetry to a local one, allowing the 8 quanta of the $SU(3)$ gauge field, called *gluons*, to mediate the strong force, successfully describing the confinement and behavior of quarks and gluons within hadrons.

The QCD Lagrangian density can be written as:

$$\mathcal{L}_{QCD} = -\frac{1}{4}F_{\mu\nu}^a F_a^{\mu\nu} + \sum_f \bar{q}_f^i (i\gamma^\mu (\mathcal{D}_\mu)_{ij} - m_f \delta_{ij}) q_f^j, \quad (1.1)$$

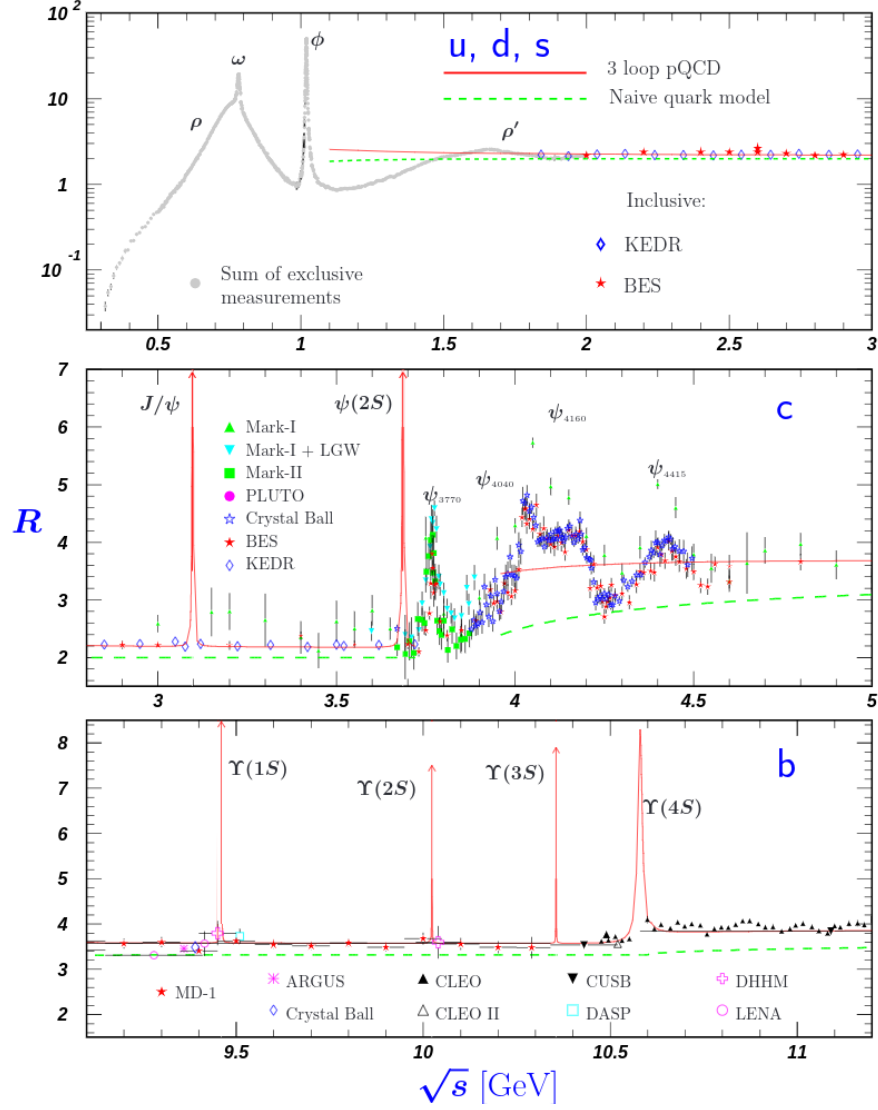


Figure 1.2: R as a function of \sqrt{s} in the light-flavor, charm, and beauty threshold regions taken from [4]. The green curve is a naive quark-parton model prediction, while the red one is a 3-loops pQCD prediction. Breit-Wigner parameterizations of J/ψ , $\psi(2S)$, and $\Upsilon(nS)$, $n = 1,2,3,4$ are also shown

where $F_{\mu\nu}^a$ is the field strength tensor defined in terms of the gluon field A_μ^a and the $SU(3)$ structure constant f^{abc} :

$$F_{\mu\nu}^a = \partial_\mu A_\nu^a - \partial_\nu A_\mu^a + g_s f^{abc} A_\mu^b A_\nu^c \quad (1.2)$$

and $(\mathcal{D}_\mu)_{ij}$ is the covariant derivative:

$$(\mathcal{D}_\mu)_{ij} = \partial_\mu \delta_{ij} - ig_s (t^a)_{ij} A_\mu^a ,$$

with t^a being one of the generators of the $SU(3)$ representation.

The last term in Eq. 1.2 is peculiar to non-Abelian theories, and gives rise to triplet and quartic gluon self-interactions illustrated in Fig. 1.3. g_s is the coupling constant, which determines the strength of the interaction between the coloured particles.

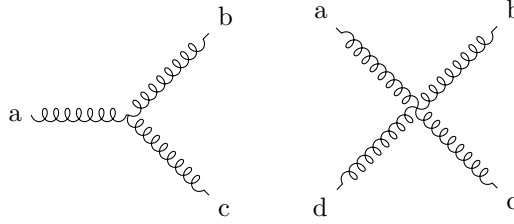


Figure 1.3: Feynman diagrams for gluons self-interactions

The second term of Eq. 1.1 describes the interactions between quarks and gluons, sketched in Fig. 1.4, and contains the mass term for the fermions. It is noteworthy to observe that the interaction between quarks and gluons is diagonal in flavor, meaning that the strong interaction conserves the flavor of quarks. In contrast, colour mixing is allowed within the framework of QCD.

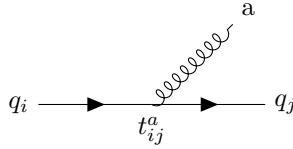


Figure 1.4: Feynman diagram for quark-gluon interaction

1.1.1 Running coupling constant

If one considers a dimensionless physical observable, denoted in the following as R , which solely depends on a single energy scale, Q , one might naturally expect that R would maintain a constant value, independent of the specific energy scale chosen. However, this does not hold true when loop diagrams are studied: the

necessity of renormalisation introduces a new energy scale denoted as μ . This scale, known as the renormalisation scale, is the point at which the subtraction of the ultraviolet divergences is carried out. Critically, μ is an arbitrary parameter and, as such, is non-physical. Consequently, R becomes dependent on the ratio Q^2/μ^2 and the renormalised coupling $\alpha_s = g_s^2/4\pi$: $R = R\left(\frac{Q^2}{\mu^2}, \alpha_s\right)$. The μ independence of R (which is an essential requirement given μ 's arbitrariness) can be expressed as:

$$\mu^2 \frac{dR\left(\frac{Q^2}{\mu^2}, \alpha_s\right)}{d\mu^2} = \mu^2 \left[\frac{\partial}{\partial \mu^2} + \frac{\partial \alpha_s}{\partial \mu^2} \frac{\partial}{\partial \alpha_s} \right] R\left(\frac{Q^2}{\mu^2}, \alpha_s\right) = 0, \quad (1.3)$$

a fundamental equation known as the renormalisation group equation. This equation is exactly true in the case of a prediction that considers all perturbative orders. If one limits the expansion at a fixed order α_s^N , then a dependence of R from μ is observed at the α_s^{N+1} order.

Solving Eq. 1.3 requires the introduction of the concept of the running coupling $\alpha_s(Q^2)$, which evolves as a function of Q . By introducing

$$t \equiv \log(Q^2/\mu^2), \quad \beta(\alpha_s) \equiv \mu^2 \frac{d\alpha_s}{d\mu^2},$$

Eq. 1.3 can be written as

$$\left(-\frac{\partial}{\partial t} + \beta(\alpha_s) \frac{\partial}{\partial \alpha_s} \right) R(e^t, \alpha_s) = 0$$

This first-order partial differential equation can be solved by defining a new function: the running coupling $\alpha_s(Q^2)$

$$t = \log(Q^2/\mu^2) \equiv \int_{\alpha_s}^{\alpha_s(Q^2)} \frac{dx}{\beta(x)}, \quad \text{with } \alpha_s = \alpha_s(\mu^2) \quad . \quad (1.4)$$

By differentiating Eq. 1.4 with respect to t and α_s , one gets:

$$\beta(\alpha_s(Q^2)) = \frac{\partial \alpha_s(Q^2)}{\partial t}, \quad \frac{d\alpha_s(Q^2)}{d\alpha_s} = \frac{\beta(\alpha_s(Q^2))}{\beta(\alpha_s)} \quad . \quad (1.5)$$

It results from this last set of equations that $R(1, \alpha_s(Q^2))$ satisfies Eq. 1.3; hence, the running coupling constant has absorbed the μ scale dependence of R . As a consequence, the knowledge of $R(1, \alpha_s)$, which can be evaluated in fixed-order perturbation theory, allows to know the dependence of R from Q^2 , which is the physical scale at which the coupling is gauged, by simply substituting $\alpha_s \rightarrow \alpha_s(Q^2)$.

The β function

The running of the coupling constant is determined by the $\beta(\alpha_s)$ function, which is evaluated from loop corrections to the bare vertices of the theory. As of the

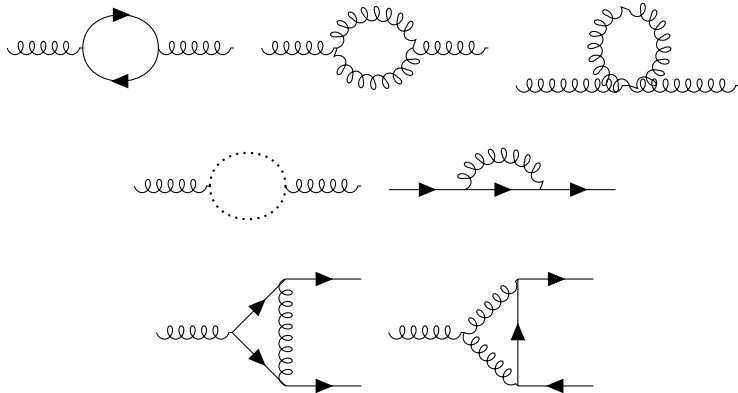


Figure 1.5: 1-loop Feynman diagrams contributing to the β function evaluation

time of the writing of this Thesis, the β function has been evaluated up to 5 loops[5]. In Fig. 1.5, the 1-loop Feynman diagrams contributing to the β function evaluation are reported.

By limiting the calculations at the first order in the perturbative expansion, one gets:

$$\beta(\alpha_s) = -\alpha_s^2 \frac{11N_c - 2N_f}{12\pi} + \mathcal{O}(\alpha_s^3) \equiv -\alpha_s^2 \beta_0 + \mathcal{O}(\alpha_s^3) \quad , \quad (1.6)$$

where N_c is the number of colours (3), while N_f is the number of quark flavours which can be considered massless at the physical scale Q^2 at which the coupling is being measured. From Eqs. 1.6 and 1.5, one can extract the Q^2 dependency of the running coupling constant:

$$\alpha_s(Q^2) = \frac{\alpha_s(\mu^2)}{1 + \alpha_s(\mu^2)\beta_0 \log(Q^2/\mu^2)} \quad , \quad (1.7)$$

Notably, since β_0 is positive also when considering 6 quark flavours, the strong coupling constant exhibits a monotonic decreasing trend as a function of Q^2 . This behaviour differs from the one of the electromagnetic coupling constant, which increases with the energy scale due to the screening effect of vacuum polarisation. For QCD, the running of the coupling constant is a direct consequence of the non-Abelian nature of the theory, allowing for gluon self-interactions, which give rise to an anti-screening effect. The idea is that the emission of virtual gluons by static colour sources causes their colour charges to 'leak out' into the surrounding vacuum. Since the interaction between distributions of charges is weaker than the one between point-like charges when the distributions overlap, the effective coupling constant decreases at short distances. This behaviour is known as asymptotic freedom, a key feature of QCD that allows for the perturbative expansion of the theory at high energy scales, where the strong coupling constant is small. At the same time, the running of the coupling

constant implies that the theory is non-perturbative at low energy scales, and phenomenological models are required to describe the strong interaction in this regime. Instead of using the renormalisation scale μ as a free parameter, one can use the running coupling constant to define a physical scale, Λ_{QCD} , which is the energy scale at which the coupling constant would diverge, if extrapolated outside the perturbative regime. Using Eq. 1.7, one can write:

$$\alpha_s(\Lambda_{QCD}) = \frac{1}{\beta_0 \log(Q^2/\Lambda_{QCD}^2)} \quad .$$

The value of Λ_{QCD} is determined by its specific definition. However, to obtain the value of the coupling constant measured at $Q^2 = M_Z^2$, an approximate value of Λ_{QCD} is around 200 MeV.

Measurements of the running of the coupling constant at different values of Q are illustrated in Fig. 1.6 and compared to the theoretical prediction at 5 loops. The agreement between the experimental data and the theoretical prediction is remarkable, confirming the validity of the QCD framework at high energy scales.

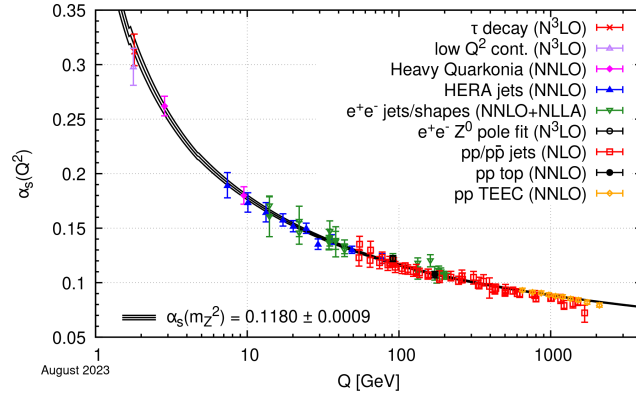


Figure 1.6: Summary of measurements of α_s as a function of the energy scale Q , compared to the running of the coupling computed at five loops, taking as an input the current PDG average, $\alpha_s(M_Z^2) = 0.1180 \pm 0.0009 \text{ GeV}/c^2$.

1.2 Confinement

The concept of confinement is one of the most intriguing aspects of QCD. It is the phenomenon by which quarks and gluons are never observed as free particles, but are always confined within colour-neutral hadrons. The confinement of quarks and gluons is a direct consequence of the non-Abelian nature of the theory, which, as described in the previous Section, is characterised by an increase of the strong coupling constant at low energy scales. This leads to the formation

of colour-neutral hadrons, which are the only particles that can be observed in nature. The confinement of quarks and gluons is a non-perturbative effect, and the theoretical description of this phenomenon is still an open question in QCD. Some phenomenological models, such as the MIT bag model, have been proposed to describe confinement, but a complete understanding of this phenomenon is still lacking. Lattice QCD simulations are the most successful approach to study the non-perturbative regime of the theory, and they have provided a wealth of information on the properties of hadrons and the strong interaction at low energy scales.

1.2.1 MIT bag model

The MIT bag model [6] is a phenomenological model of confinement, which describes hadrons as bound states of quarks and gluons confined within a finite volume, called the bag. The model was developed in the 1970s by A. Chodos, R. L. Jaffe, K. Johnson, C. B. Thorn, and V. F. Weisskopf, and it has been widely used to study the properties of hadrons and the strong interaction. In the MIT bag model, N massless fermions are confined within a spherical cavity of radius R , which is the bag radius. The confinement arises from a balance between pressure due to the kinematic energy of the fermions inside the bag and an ad hoc external pressure, which is introduced to confine the fermions within the bag. The fermions are described by the Dirac equation for massless fermions:

$$i\gamma^\mu \partial_\mu \psi = 0 \quad ,$$

where ψ is the fermion field, and γ^μ are the Dirac matrices. The solution to the Dirac equation is given in terms of the spherical Bessel functions of the zeroth and first order, $j_0(p_0 r)$ and $j_1(p_0 r)$, where p_0 is the energy of the fermion:

$$\psi = \mathcal{N} e^{-ip_0 t} \begin{pmatrix} j_0(p_0 r) \chi^+ \\ \vec{\sigma} \cdot \hat{r} j_1(p_0 r) \chi^- \end{pmatrix} \quad ,$$

where χ^+ and χ^- are the two components of the fermion four dimensional spinor ψ , and $\vec{\sigma}$ are the Pauli matrices. The colour flux at a point r inside the bag is given by:

$$j_{ab}^\mu(r) = \bar{\psi}_a(r) \gamma^\mu \psi_b(r) \quad ,$$

where a and b are the colour indices of the fermions. If the quantum numbers are not to be lost through the surface of the bag, which is the definition of confinement, then:

$$n_\mu j_{ab}^\mu(r) = \bar{\psi}_a(r) \gamma \cdot n \psi_b(r) = 0 \quad ,$$

on the surface, where n is a unit space-like vector normal to the surface. Using the gamma properties, $(i\gamma \cdot n)^2 = 1$, so that by assuming that $i\gamma \cdot n = +1$, the boundary condition on the surface of the bag is given by:

$$\bar{\psi}(R)\psi(R) = 0 \quad ,$$

leading to the solution of the Dirac equation in the bag:

$$[j_0(p_0 R)]^2 - [j_1(p_0 R)]^2 = 0 \quad ,$$

with solution $p_0 R = 2.04$. The total energy inside the bag is given by:

$$E = \frac{2.04N}{R}(\hbar c) + \frac{4\pi}{3}R^3 B \quad ,$$

where the first term is the kinetic energy of the fermions, and the second term is the energy due to the presence of an external pressure B which keeps the fermions confined in the bag. The bag pressure is a phenomenological parameter of the model, and it is introduced to confine the fermions within the bag. It can be extracted by minimising the energy of the system with respect to the bag radius R , yielding $B = 234 \text{ MeV/fm}^3$, for a baryon with $R = 0.8 \text{ fm}$.

1.2.2 Lattice QCD

Lattice QCD is a numerical technique used to study the non-perturbative regime of QCD. The method is based on the discretisation of spacetime on a four-dimensional lattice, and the evaluation of the path integral of the theory by Monte Carlo methods, i.e. by sampling possible configurations of the quark and gluon fields according to the probability distribution given by the QCD Lagrangian. The lattice spacing is a parameter of the method, and allows one to avoid the ultraviolet divergences of the theory, which are typical in perturbative QCD, by introducing a cutoff on the momenta of the quark and gluon fields. The Lattice QCD simulations are based on the path integral formalism of quantum field theory [7], developed by R. Feynman in the 1940s. The path integral provides a natural extension of the least action principle of classical mechanics to quantum mechanics, and it allows one to calculate the probability amplitude of a particle to move from one point to another in spacetime, considering the evolution of the system over all possible paths. The transition amplitude from the state (x_a, t_a) to the state (x_b, t_b) is given by:

$$A[(x_a, t_a) \rightarrow (x_b, t_b)] = \langle x_b, t_b | e^{-iH(t_b - t_a)} | x_a, t_a \rangle = \sum_{\text{paths}} e^{iS[x(t)]} \quad , \quad (1.8)$$

where H is the Hamiltonian of the system, $S[x(t)]$ is the action of the system, and the sum is over all possible paths from (x_a, t_a) to (x_b, t_b) . By taking the continuum limit on space-time, we obtain an integration over all the possible space-time paths of the system:

$$\sum_{\text{paths}} e^{iS[x(t)]} \rightarrow \int_{x_a}^{x_b} [\mathcal{D}x(t)] e^{iS[x(t)]} \quad , \quad (1.9)$$

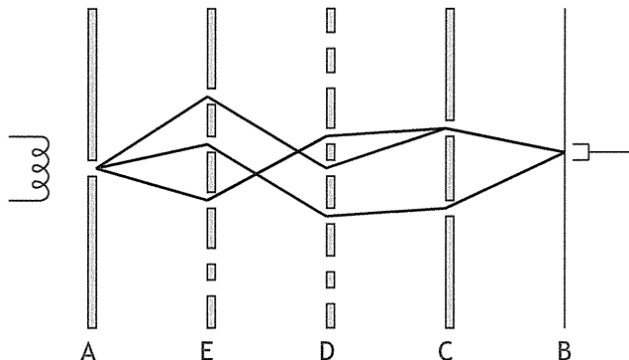


Figure 1.7: Feynman introduction to path integrals. Here, a particle emitted from a source at x_a is detected at x_b . A finite number of screens, each with a finite number of holes, is placed between the source and the detector. The probability amplitude for the particle to hit the detector is given by the sum of the probabilities of moving from the source to the detector through all possible paths. By adding an infinite amount of screens with an infinite number of holes, and by also considering the time at which the particle passes through the screens, the sum becomes an integral over all possible paths, called a *path integral*.

where the right-hand side term is a functional integral over all possible paths of the system. It is interesting to note that by combining Eqs. 1.8 and 1.9, one gets a quantity resembling the partition function of a statistical system:

$$\mathcal{Z} = \sum_{x_a} \langle x_a, t_a | e^{\beta H} | x_a, t_a \rangle \quad .$$

It is possible to express the partition function in terms of a path integral by applying a Wick rotation to the time variable, $t \rightarrow -i\tau$, with $\tau_a = 0 \leq \tau \leq \tau_b = \beta$ and considering the Euclidean action in place of the Minkowskian one, $S_E = iS$. Furthermore, since the state at τ_a is the same as the one at τ_b , a periodic boundary condition is imposed: $x(\tau_a) = x(\tau_b)$. With these considerations, the partition function can be expressed as:

$$\mathcal{Z} = \int [\mathcal{D}x(\tau)] e^{-S_E[x(\tau)]} \quad .$$

This formalism, which was here developed for a single particle, can be extended to a quantum field theory, and in particular to QCD.

The lattice QCD simulations are computationally intensive, and they require large supercomputers to perform the calculations. To limit the computational costs, calculations are often performed at larger up and down quark masses than in nature, drastically reducing the number of virtual quark-antiquark loops that have to be taken into account. Because of the employed Monte Carlo approach,

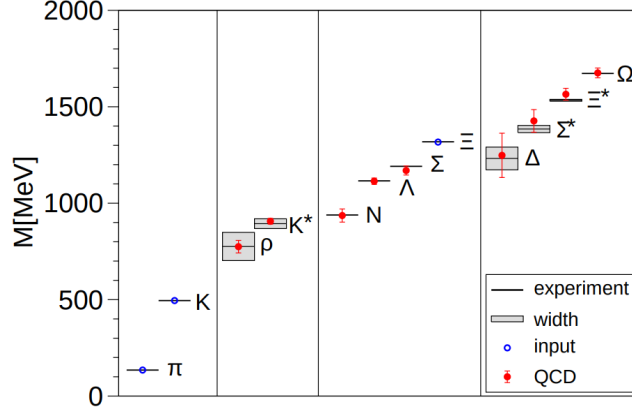


Figure 1.8: The light hadron spectrum of QCD. Horizontal lines and bands are the experimental values with their decay widths. Lattice QCD results [8] are shown by solid circles. Vertical error bars represent the combined statistical and systematic error estimates. π , K and Ξ have no error bars, because they are used to set the light quark mass, the strange quark mass, and the overall scale, respectively.

only a finite number of configurations can be considered, leading to statistical uncertainties in the lattice QCD results. In order to obtain physical results, several limits have to be taken: i. the continuum limit, i.e. the extrapolation of the lattice spacing to zero, ii. the infinite-volume limit, i.e. the extrapolation of the lattice size to infinity, and iii. the physical quark-mass limit, i.e. the extrapolation to physical quark masses, although many present-day lattice calculations are already performed directly at, or very close to, the physical values of the quark masses, so that the latter extrapolation becomes less of an issue.

The results of the lattice QCD simulations are in good agreement with the experimental data, and they have provided valuable insights into the properties of the strong interaction at low energy scales. For example, Fig. 1.8 shows the spectrum of hadrons obtained from lattice QCD simulations, taken from [8], compared to the experimental data. The agreement between the lattice QCD results and the experimental data is remarkable, confirming the validity of the QCD framework at low energy scales.

1.3 Quark Gluon Plasma

The concept of deconfinement refers to the transition from a confined state to a state where quarks and gluons are no longer confined within hadrons, but are free to move in a larger volume. As modelled by the MIT bag model, non-perturbative QCD effects can be described in terms of an external pressure, which confines quarks and gluons within a finite volume. If the external pressure

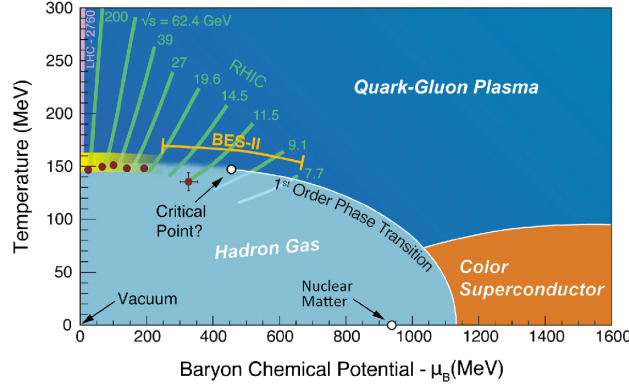


Figure 1.9: QCD phase diagram in the temperature-baryon chemical potential plane.

is overcome by the pressure due to the kinematic energy of the quarks and gluons, then the hadrons constituents are no longer confined, and a transition to a state called Quark-Gluon Plasma (QGP) occurs. Lattice QCD calculations are used to understand the properties of the QGP, and they predict that a strongly interacting system with zero net baryon density evolves smoothly from a confined (hadronic) towards a deconfined (quarks and gluons) state when its temperature is increased up to ~ 155 MeV (1.8×10^{12} K) [9, 10], reaching energy densities of ~ 1 GeV/fm³.

It is believed that the universe underwent a phase of deconfinement in the early stages of its evolution, a few microseconds after the Big Bang. Direct observation of the primordial QGP (i.e. that created just after the Big Bang) would provide a wealth of information on the early universe; however, the universe experienced a phase in which electrons were not bound to nuclei, making it opaque to electromagnetic radiation, and denying us the possibility of directly observing the QGP. Once the universe cooled enough (3000 K) to allow electrons to bind to nuclei, the electromagnetic radiation decoupled with a black body spectrum of around 3000 K. Since then, as the universe expanded, this electromagnetic radiation has redshifted to a temperature of around 2.7 K, and is denoted as the Cosmic Microwave Background (CMB). The CMB is the oldest light in the universe and provides a snapshot of the universe when it was 300,000 years old, long after the QGP had already cooled down. Hence, the only way to study the QGP is by recreating it in the laboratory, through the collision of heavy ions at high energies. In the past decades, several experiments [11, 12, 13, 14] have been carried out to study the properties of this state of matter, and the results have provided valuable insights into the properties of the strong interaction at high energy scales.

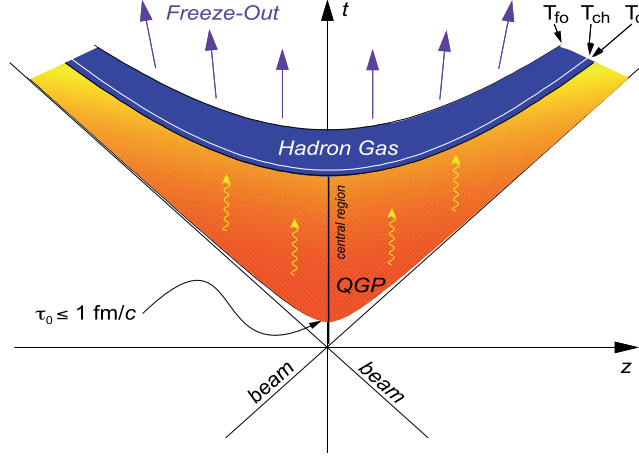


Figure 1.10: Space-time evolution of a heavy-ion collision.

1.3.1 Heavy-ion collisions

Heavy-ion collisions are the most suitable environment to study the properties of the QGP. In these collisions, two heavy ions, such as lead or gold nuclei, are accelerated to ultra-relativistic energies and made to collide head-on. Given the large amount of energy deposited in the collision, the system reaches high energy densities of around 16 GeV/fm^3 after 1 fm/c [15], which allows for the production of the QGP. As nuclei are objects made of many nucleons (i.e. protons and neutrons), the interaction volume (called *fireball*) is larger and longer-lived than in proton-proton collisions, allowing to use thermodynamics and fluidodynamics to describe the system.

The collision of two nuclei is a rather complex process, with a space-time evolution that can be divided into several stages, as depicted in Fig. 1.10. It is possible to distinguish between two different collision regimes. When the centre-of-mass energy per nucleon pair ($\sqrt{s_{NN}}$) is below a few GeV, the nucleons are stopped in the collision as they lose energy and momentum. Due to conserved currents, the quantum numbers of the initial state are preserved, so that, for example, the net baryon production (i.e. the difference between the number of baryons and antibaryons) is positive. This regime is called *stopping regime*. When the $\sqrt{s_{NN}}$ increases, the initial state baryon number is carried away by the receding nucleons, and the net baryon number in the fireball is zero. This regime is denoted as *Bjorken regime*, or *transparency regime*.

As anticipated above, the space-time evolution of the created system can be divided into several stages. They can be studied by measuring different final-state observables that are correlated to such stages. One of the first descriptions of the fireball evolution was given by Bjorken [16], who proposed a simple model to describe the expansion of the system in the longitudinal direction. In this model, it is assumed that there exists a central-plateau structure in the inclusive

particle productions as a function of the rapidity variable, which is defined as

$$y = \frac{1}{2} \log \left(\frac{E + p_z}{E - p_z} \right) ,$$

where E is the energy and p_z is the longitudinal momentum of the particle. In other terms, the Bjorken model assumes that the system is boost-invariant, i.e. independent of the longitudinal velocity. According to this model, the evolution of the system is described by the following stages: i. collision of the two nuclei, ii. pre-equilibrium, iii. QGP formation, iv. hadronisation, and v. freeze-out.

Collision

The two nuclei are accelerated to ultra-relativistic energies and are thus Lorentz-contracted in the direction of motion. The collision takes place in a very short time $\tau_{\text{coll}} = 2R/\gamma$, where R is the nucleus radius and γ the Lorentz factor. At LHC energies, the nuclei crossing time is of ~ 0.005 fm/ c , which is much smaller than the time scale of the strong interaction $\tau_{\text{strong}} \sim 1/\Lambda_{QCD} \sim 1$ fm/ c . Particles produced in the collision through parton interactions mediated by the strong force are thus created once the colliding nuclei have already passed through each other and moved away from the interaction region. During the collision, a large amount of energy is deposited in the interaction region, leading to the formation of a fireball with high energy densities.

Pre-equilibrium

After τ_{coll} , secondary particles are produced from the energy deposited in the collision. In the Bjorken regime, it is possible to evaluate the energy density of the system as a function of time by measuring the transverse energy of the particles produced at midrapidity, where the net baryon density is zero. The energy density is given by:

$$\varepsilon_{\text{Bjorken}} = \frac{\langle m_T \rangle}{\tau A} \frac{dN}{dy} \Big|_{y=0} = \frac{1}{\tau A} \left\langle \frac{dE_T}{dy} \right\rangle \Big|_{y=0} ,$$

where A is the transverse area collision region, $\langle m_T \rangle$ is the mean transverse mass, defined as $m_T = \sqrt{m^2 + p_T^2}$, N is the number of secondary particles, and $\langle dE_T/dy \rangle$ is the mean transverse energy density. It is interesting to evaluate the energy densities reached at the time of particle formation, which can be estimated using Heisenberg's uncertainty principle: $\tau = \hbar/m_T$. the mean transverse mass of the particles produced in the collision can be evaluated using the approximate formula:

$$\langle m_T \rangle = \frac{\frac{dE_T(\tau_f)}{dy}}{\frac{dN(\tau_f)}{dy}} \sim \frac{\frac{dE_T}{d\eta}}{\frac{dN}{d\eta}} \Big|_{\text{final state}} ,$$

which leads to a formation time of ~ 0.35 fm/ c at RHIC [17], to which corresponds an energy density of ~ 15 GeV/fm³.

Quark-gluon plasma formation

The system of produced particles reaches thermal equilibrium through multiple scatterings at a proper time τ_{eq} , and the QGP is formed. Its evolution can be described using relativistic hydrodynamics, which can be used to predict τ_{eq} . Studies at RHIC allowed to constrain τ_{eq} in the range of $0.6 < \tau_{\text{eq}} < 1$ fm/c, corresponding to energy densities of $5.4 < \varepsilon_{\text{Bjorken}}(\tau_{\text{eq}}) < 9$ GeV/fm³, which are consistent with what is expected for QGP formation.

Hadronisation

The deconfined system expands and cools down, until the temperature decreases below the pseudo-critical value for the transition crossover. The QGP undergoes a phase transition and hadronises, producing an expanding gas of colour-neutral particles. At LHC energies, this is expected to happen ~ 10 fm/c after the QGP formation. This transition is associated with a sharp decrease in the entropy density of the system.

Freeze-out

During the hadron gas expansion, the particle density decreases to a point where the inelastic interactions cease. The moment in which this happens is called *chemical freeze-out*, and takes place at around $T_{\text{chem}} \sim 160$ MeV [18]. The chemical abundances of the hadron gas cannot vary anymore, although elastic interactions, which change the momentum spectrum of the produced particles still occur. Once the temperature decreases below $T_{\text{therm}} \sim 130$ MeV, the elastic interactions cease as well, and this is referred to as *thermal freeze-out*. The particles then keep expanding without interactions (*free-streaming*), and are detected by the experimental apparatus.

1.3.2 Radial flow

After the chemical freeze-out, inelastic interactions between the hadrons do not take place anymore. However, elastic interactions can still occur, leading to a modification of the momentum distribution of the particles. By studying the transverse momentum spectra of the particles produced in the collision, it is possible to extract information on the produced system.

For a stationary thermal source with a temperature T , the Lorentz-invariant momentum distribution of the particles is given by:

$$E \frac{dN}{d^3p} = \frac{dN}{p_T dp_T d\varphi dy} = \frac{g_i V}{(2\pi)^3} E \frac{1}{e^{(E-\mu_i)/T} \pm 1} \quad ,$$

where E is the energy of the particle, g_i is the degeneracy factor, V is the volume of the source, μ_i is the chemical potential of the particle of species i , and the $+$ sign is for fermions while the $-$ sign is for bosons. By using the relation

$$\frac{dN}{p_T dp_T} = \frac{dN}{m_T dm_T} \quad ,$$

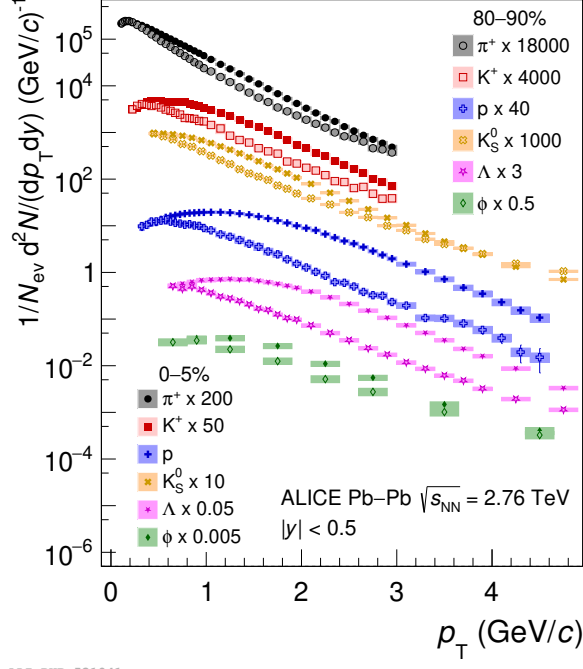


Figure 1.11: Transverse momentum distributions of π^+ , K^+ , p , K_S^0 , Λ , and ϕ mesons for the 0–5% and 80–90% centrality intervals in Pb–Pb collisions at $\sqrt{s_{NN}} = 2.76 \text{ TeV}$. The data points are scaled by various factors for better visibility.

and by assuming that $e^{(E-\mu_i)/T} \gg 1$, the transverse momentum spectrum of particles can be obtained by integrating over the azimuthal angle φ and the rapidity y , leading to:

$$\frac{dN}{m_T dm_T} = \frac{g_i V}{(2\pi)^2} m_T e^{\mu_i/T} K_1\left(\frac{m_T}{T}\right) \xrightarrow{m_T \gg T} V' \sqrt{m_T} e^{-m_T/T} \quad . \quad (1.10)$$

From Eq. 1.10 emerges that for a stationary thermal particle source with a temperature T , the transverse mass spectrum of the particles follows an exponential distribution, with a slope parameter T , and is independent of the particle species. This is known as the m_T -scaling of the transverse mass spectra, and is observed in pp and small-system collisions at low \sqrt{n} , with a slope parameter of $T \sim 167 \text{ MeV}$. However, in heavy-ion collisions, this description is not valid, as the QGP has a thermal pressure, since it is a thermalised system of deconfined quarks and gluons. The pressure difference between the QGP and the surrounding vacuum leads to a collective expansion of the fireball, which

is called *radial flow*. This causes the particles to be pushed in the transverse direction, leading to a modification of the transverse momentum spectra of the particles, which is characterised by a shift of the spectra towards higher p_T values, with a more pronounced effect for heavier particles, as shown in Fig. 1.11. The radial flow can also be defined as a correlation between the velocity of an element of the system and its space-time position, which is superimposed on the random thermal motion of the particles.

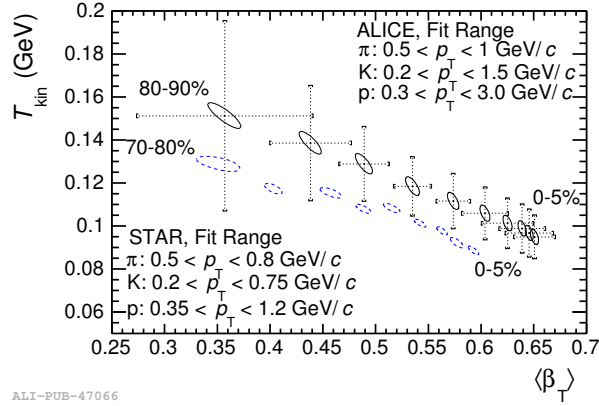


Figure 1.12: Results of blast-wave fits obtained with the ALICE experiment at the LHC, compared to similar fits at RHIC energies, for different centrality intervals.

The radial flow can be described by using phenomenological models, such as the blast-wave model [19], which assumes that the particles are emitted from a thermal source with a collective velocity field. It relies on the Cooper-Frye prescription [20], which assumes an instantaneous freeze-out of the particles in the radial direction, to calculate the transverse momentum spectra of the particles in terms of the temperature of the source, the collective velocity field, and the transverse flow profile. Results from SPS, RHIC, and LHC experiments show that the transverse momentum spectra of the particles produced in heavy-ion collisions can be well described by the blast-wave model, with a temperature of the source of around 110–120 MeV, almost independent of the centre-of-mass energy per nucleon pair, and a collective velocity field of around 0.5–0.6 c in the most central collisions, with a growing trend with $\sqrt{s_{NN}}$, as shown in Fig. 1.12. Although the blast-wave model provides a good description of the transverse momentum spectra of the particles produced in heavy-ion collisions, it is important to note that the parameters which are evaluated with this model are extracted by fitting the m_T spectra of the particles, and could not be directly related to the properties of the QGP. Hence, it is important to study whether more sophisticated models, such as hydrodynamics, can provide a more detailed description of the space-time evolution of the system.

Hydrodynamics-based models rely on energy and momentum conservation laws, which need to be expressed in a relativistic form since the expansion of the system is relativistic:

$$\partial_\mu T^{\mu\nu} = 0 \quad , \quad \text{with} \quad T^{\mu\nu} = (\varepsilon + p)u^\mu u^\nu - pg^{\mu\nu} \quad ,$$

where $T^{\mu\nu}$ is the energy-momentum tensor, ε is the energy density, p is the pressure, u^μ is the four-velocity of the fluid element, and $g^{\mu\nu}$ is the metric tensor. An additional condition comes from the conservation of the baryon number, which is expressed as:

$$\partial_\mu (n_B u^\mu) = 0 \quad ,$$

where n_B is the baryon density. A further equation is needed to close the system, which is provided by the equation of state of the QGP, which relates the pressure to the energy density and the baryon density. As the fireball is in a non-equilibrium state in the early stages of the collision, the hydrodynamics equations need an initial condition to describe the system. This is usually provided by the Glauber model [21], which describes the collision of the two nuclei as a superposition of nucleon-nucleon collisions, and provides the initial energy density profile of the system. Monte Carlo simulations describing partonic showers such as UrQMD [22] and AMPT [23] can also be used to provide the initial conditions for the hydrodynamics models.

The hydrodynamics calculations provide a good description of the transverse momentum spectra of the particles produced in heavy-ion collisions, and the emerging parameters are similar to those obtained with the blast-wave model. In addition, hydrodynamics calculations and their extensions, such as viscous hydrodynamics, can be used to study other observables, such as the elliptic flow, which is a measure of the anisotropy of the particle emission in the transverse plane.

1.3.3 High- p_T hadrons and jet quenching

High- p_T partons are produced in hard-scattering processes, i.e. those with a high momentum transfer. As such, they are typically produced in the early stages of the collision and experience the whole fireball evolution. They can therefore be used to probe the properties of the earliest stages of the QGP. The Glauber model predicts the production cross-section of hard-scattering processes to scale with the number of binary nucleon-nucleon collisions. To test this prediction, the nuclear modification factor, R_{AA} , is defined as the ratio of the p_T -differential hadron yield in heavy-ion collisions to the one in proton-proton collisions, scaled by the mean number of binary nucleon-nucleon collisions $\langle N_{\text{coll}} \rangle$:

$$R_{AA} = \frac{dN_{AA}/dp_T}{\langle N_{\text{coll}} \rangle dN_{pp}/dp_T} \quad .$$

As the p_T increases, the production mechanism becomes harder, and it is expected that the nuclear modification factor approaches unity, namely binary

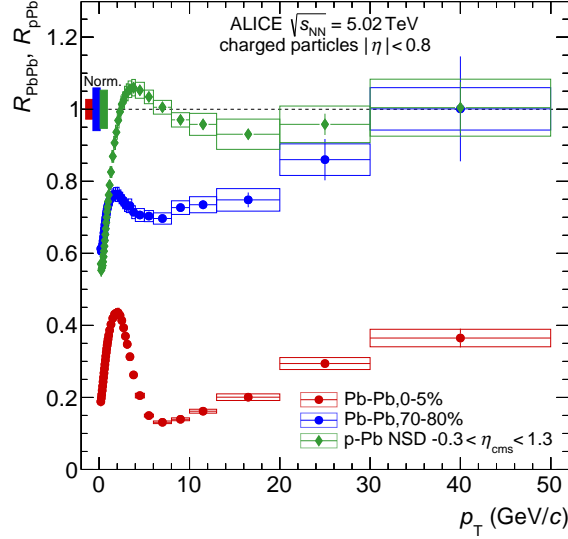


Figure 1.13: Nuclear modification factors measured by ALICE in central (0–5%) and peripheral (70 – 80%) Pb–Pb collisions at $\sqrt{s_{NN}} = 13$ TeV and in p–Pb collisions at $\sqrt{s_{NN}} = 13$ TeV.

scaling. However, experimental results [24] show that the nuclear modification factor is suppressed at high p_T , with a suppression that increases with the centrality of the collision. This suppression is due to both initial-state effects, such as the Cronin effect [25], which can be studied in proton-nucleus collisions where the production of QGP is not expected, and to final-state effects, due to the presence of the QGP. Partons traversing the QGP lose energy through elastic scatterings with the partons of the medium, and via gluon radiation, which is the dominant process for high-energy partons. The energy loss can be estimated in the BDMPS formalism [26], which assumes that the radiated gluon gets decoherent from the parton through multiple soft scatterings with the medium constituents. The energy loss of the partons is quantified as:

$$\Delta E = \frac{1}{4} \alpha_s C_R \hat{q} L^2 \quad ,$$

Where α_s is the strong coupling constant, C_R is the Casimir factor, which is 3 for gluon-gluon couplings and 4/3 for quark-gluon interactions, \hat{q} is the transport coefficient, and L is the path length of the parton in the medium. The transport coefficient is related to the energy-density of the medium, as $\hat{q} \propto \varepsilon^{3/4}$, so that energy loss measurements can be used to infer the properties of the QGP. Typical energy losses of high- p_T partons traversing the whole QGP are of the order of 40 GeV, which is a significant fraction of the parton energy.

The energy loss of the partons leads to a suppression of the high- p_T hadron spectra, which consequently leads to a suppression of the nuclear modification factor at high p_T .

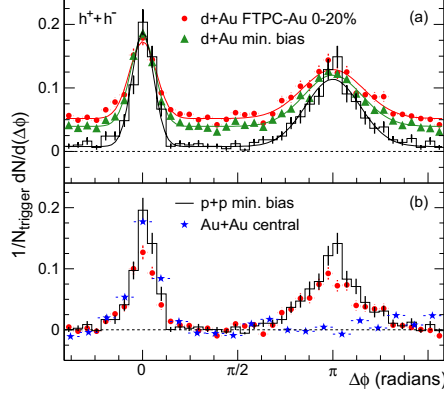


Figure 1.14: Top: Two-particle azimuthal distributions for minimum bias and central d–Au collisions, and for proton-proton collisions at $\sqrt{s_{NN}} = 200$ GeV measured by the STAR Collaboration. Bottom: Comparison of pedestals-subtracted two-particle azimuthal distributions for central d–Au collisions to those seen in proton-proton and central Au–Au collisions.

At leading order, partons are produced in back-to-back pairs, forming what is known as di-jets. The parton shower generated by the jet pointing in the direction of the medium is expected to lose more energy than the one pointing in the opposite direction, leading to what is known as *jet quenching*. These interactions can be studied by measuring two-particle azimuthal distribution correlations of the produced hadrons. For each event, the particle with the highest p_T above a certain threshold is selected, and the azimuthal angle of other high- p_T particles is measured with respect to the first one. For proton-proton and proton-nucleus collisions, the azimuthal distribution presents two peaks: the *near-side peak*, which is found at $\varphi = 0$ and is due to the hadrons produced in the same jet as the trigger particle, and the *away-side peak*, which is found at $\varphi = \pi$ and is due to the hadrons produced in the opposite jet. In heavy-ion collisions, the away-side peak is suppressed due to the energy loss in the QGP, as shown in Fig. 1.14.

In addition, the QGP can also affect the hadronisation process. In small colliding systems, such as pp and p–Pb collisions, hadronisation occurs via fragmentation, where the colour string holding together a quark-antiquark pair breaks, producing a quark-antiquark pair. This process leads to the production of a collimated jet of hadrons with a p_T which is lower than the one of the first quark-antiquark pair. When the QGP is produced, another hadronisation mechanism becomes available, because the QGP is a thermalised system: the coalescence (or recombination) mechanism. Low p_T partons close in the velocity-space phase space can bind together to form a higher- p_T hadron. This

enhances the production of baryons, as the p_T -distribution of partons inside the QGP follows a rapidly decreasing trend.

1.3.4 Strangeness enhancement

One of the first proposed signatures of the QGP formation is the strangeness enhancement [27], which refers to the observation of an increased production of strange hadrons in heavy-ion collisions compared to proton-proton collisions. At a microscopic level, the enhancement of strange hadrons is a direct consequence of the high energy densities reached in the collisions, which allow for the thermal production of strange quarks and antiquarks. Strange quarks are not present as valence quarks in the initial state, and can be produced in hard $2 \rightarrow 2$ scatterings ($gg \rightarrow s\bar{s}, q\bar{q} \rightarrow s\bar{s}$), or via gluon splitting ($g \rightarrow s\bar{s}$) during the evolution of the system. While these processes are dominant for the production of strange hadrons with high p_T , at low p_T the production of strange hadrons is dominated by non-perturbative processes. At a macroscopic level, the enhancement of the production of strange hadrons can be explained using a statistical approach, in a framework known as the statistical hadronisation model. In this model, the system is described as an ideal gas of hadrons and resonances, which is assumed to be in thermal and chemical equilibrium at the chemical freeze-out. The hadrons production in heavy-ion collisions is described according to a grand-canonical ensemble statistical distribution, which depends on the temperature and the chemical potentials of the system. In a grand-canonical ensemble, which is used to describe a system that exchanges both energy and particles with a reservoir, the energy and quantum numbers are only conserved on average on a large volume. The description of the hadrons production in smaller colliding systems, such as e^+e^- and pp collisions, requires the use of a canonical ensemble, which is used to describe a system that exchanges only energy with a reservoir, and requires the exact (local) conservation of the quantum numbers. This leads to a suppression of strange quark production as compared to the grand canonical ensemble.

The strangeness enhancement in heavy-ion collisions has been observed in several experiments, such as the STAR experiment at RHIC [28] and the ALICE experiment at the LHC [29]. In addition, an enhancement of strange hadrons has been observed in small systems, such as pp [30] and p-Pb [31, 32] collisions, in high-multiplicity events, and follows a hierarchy determined by the hadron strangeness. This observation is intriguing, as QGP production is not expected in such systems. Furthermore, several effects such as azimuthal correlations and mass-dependent hardening of p_T distributions, which are typically associated with QGP formation in nuclear collisions, have been observed in these systems. Could small droplets of QGP be formed in these collisions? Could other mechanisms explain the observed effects? These are still open questions in the field of high-energy nuclear physics, and they are the subjects of ongoing research.

Figure 1.15 shows the p_T -integrated yield ratios of strange (K_s^0, Λ) and multi-strange (Ξ^\pm, Ω^\pm) hadrons to pions ($\pi^+ + \pi^-$) as a function of the charged particle

multiplicity density, $\langle dN_{\text{ch}}/d\eta \rangle$, measured in $|y| < 0.5$ in different collision systems (pp, p-Pb and Pb-Pb) using the ALICE experiment at the LHC [30]. The data show a clear enhancement of strange to non-strange hadron production with increasing multiplicity. At the highest multiplicities, the yield ratios saturate at values that are compatible with what is measured in central Pb-Pb collisions, where QGP is formed.

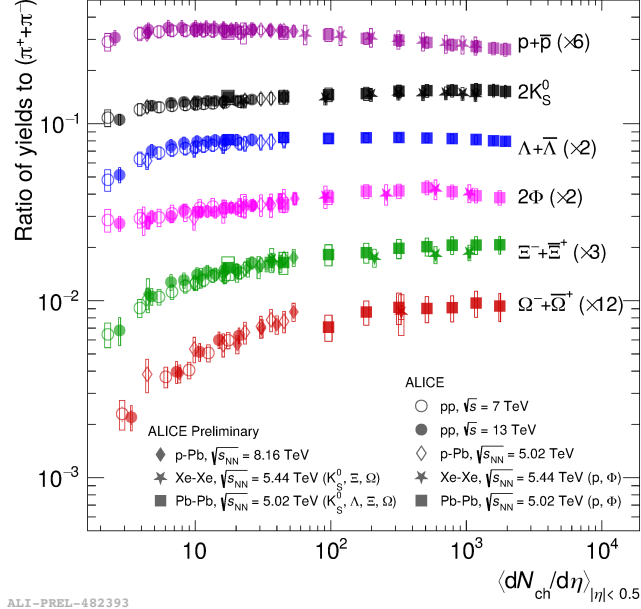


Figure 1.15: p_T -integrated yield ratios of strange (K_s^0 , Λ) and multi-strange (Ξ^\pm , Ω^\pm) hadrons to pions ($\pi^+ + \pi^-$) as a function of $\langle dN_{\text{ch}}/d\eta \rangle$ measured in pp, p-Pb and Pb-Pb collisions at midrapidity ($|y| < 0.5$).

Chapter 2

Open heavy-flavour production in pp collisions

Open heavy-flavour hadrons, i.e. those in which the heavy quark quantum number is expressed, made of one charm or beauty quark and other lighter quarks (such as D-mesons and B-mesons), can only be produced in processes with a high momentum transfer, because of the large mass of about 1.27 GeV and 4.18 GeV of the charm and beauty quarks, respectively. As such, they are created in the early stages of the collision, and their production cross-section in the partonic interaction can be evaluated perturbatively using QCD. The study of the production of open heavy-flavour hadrons in proton-proton collisions therefore provides an important test of the perturbative QCD framework and allows setting constraints on the models parameters. In addition, measurements of the production of open heavy-flavour hadrons in proton-proton collisions, where the production of a deconfined medium is not expected due to the low energy densities reached, are necessary ingredients for the study of heavy-ion collisions, where the properties of the QGP can be investigated.

2.1 Factorisation theorems

The production of open heavy-flavour hadrons in proton-proton collisions can be described using the factorisation theorems [33], which allow separating the short-distance, perturbative behaviour from the long-distance, non-perturbative one. The total production cross-section can be expressed as:

$$\sigma_{pp} = \sum_{a,b=g,q,\bar{q}} \int dx_1 dx_2 f_{a/A}(x_1, \mu_F^2) f_{b/B}(x_2, \mu_F^2) \hat{\sigma}_{ab \rightarrow c}(x_1, x_2, \mu_F^2, \mu_R^2) D_{c \rightarrow H}(z, \mu_F^2) \quad ,$$

i.e. the convolution of; i. the Parton Distribution Functions (PDFs) $f_{a/A}(x_1, \mu_F^2)$ and $f_{b/B}(x_2, \mu_F^2)$, which describe the probability of finding a parton a in the proton A carrying a fraction of the proton momentum x_1 , and a parton b in

the proton B with a momentum fraction x_2 , respectively; ii. the hard partonic scattering cross-section $\hat{\sigma}_{ab \rightarrow c}(x_1, x_2, \mu_F^2, \mu_R^2)$, which describes the probability of producing the final state c from the collision of the partons a and b ; and iii. the Fragmentation Functions (FFs) $D_{c \rightarrow H}(z, \mu_F^2)$, which describe the probability of a parton of type c fragmenting into a heavy-flavour hadron H with a momentum fraction z . While the PDFs and FFs are non-perturbative quantities, measured from data and then considered universal across different processes, the hard partonic scattering cross-section can be calculated perturbatively using QCD, but needs to be evaluated for each process. The factorisation theorems have been widely used to describe the production of open heavy-flavour hadrons in proton-proton collisions, and have proven to be successful in describing the data. Figure 2.1 shows the production cross-section of prompt and non-prompt D^0 -mesons in proton-proton collisions at $\sqrt{s} = 13$ TeV at midrapidity ($|y| < 0.5$) as a function of the transverse momentum p_T measured by the ALICE experiment [34], compared to FONLL calculations [35]. The term *prompt* refers to charm-hadrons produced directly in the hadronisation of a charm quark or the strong decay of a directly produced excited charm-hadron state, in contrast to *feed-down* charm-hadrons, produced in the decay of a hadron containing a beauty quark. The FONLL predictions are in good agreement with the non-prompt D^0 -meson production cross-section, while the prompt contribution lies on the upper edge of the theoretical uncertainty band, albeit it is described within the uncertainties. This trend is also observed in the production of other open heavy-flavour hadrons and different experimental facilities, such as Tevatron, RHIC and LHC.

2.1.1 Parton Distribution Functions

Deep inelastic scattering

The PDFs are non-perturbative quantities that describe the probability of finding a parton with a fraction x of the proton momentum in the initial state of the process. The discovery that the proton is made of partons, i.e. quarks and gluons, was a fundamental step in the development of this framework. The experiment that provided the first evidence of the partonic structure of the proton was the deep inelastic scattering experiment carried out at the Stanford Linear Accelerator Center (SLAC) in the 1960s [37], where an electron was scattered off a proton, and the momentum transfer was measured. Figure 2.2 shows the kinematics of an inelastic scattering process, where the electron with momentum p_e scatters off the nucleon with momentum P and mass M , and the electron with momentum p'_e is detected. The momentum transfer q is defined as $q = p_e - p'_e$, and the invariant mass of the system X is given by $q^2 = -Q^2$. The mass of the final hadronic state X is given by

$$M_X^2 = P_X^2 = (P + p_e - p'_e)^2 = (P + q)^2 = M^2 + 2P \cdot q + q^2 = M^2 + 2M\nu - Q^2 \quad ,$$

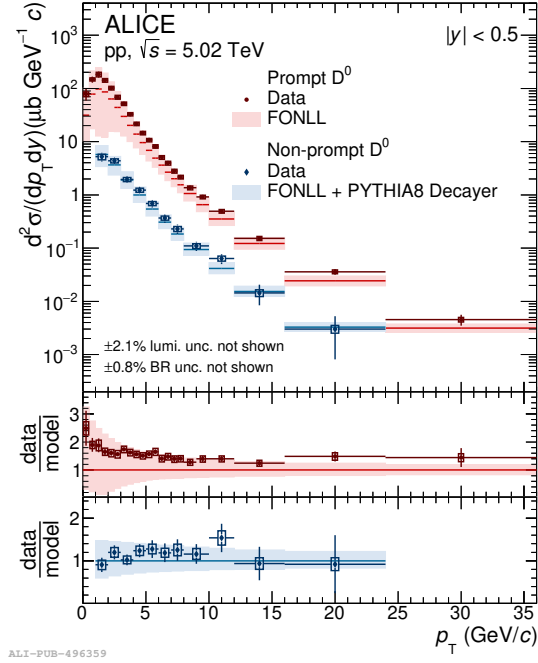


Figure 2.1: p_T -differential production cross-section of prompt and non-prompt D^0 -mesons [34] compared to predictions obtained with FONLL calculations [35] combined with PYTHIA 8 [36] for the $H_b \rightarrow D^0 + X$ decay kinematics.

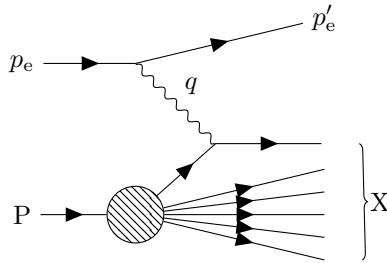


Figure 2.2: Caption

having defined

$$q = p_e - p'_e \quad , \quad \nu = \frac{P \cdot q}{M} \quad , \quad Q^2 = -q^2 \quad .$$

ν is the energy transfer in the proton rest frame, and defines the inelasticity of the process when combined with information on Q and M . The elastic limit corresponds to $M_X^2 = M^2$, i.e. $2M\nu = Q^2$; when resonant states with mass M_R are excited, then $M_X^2 = M_R^2$, and $2M\nu = Q^2 + M_R^2 - M^2$; inelastic scattering are found for $0 < \frac{Q^2}{2M\nu} < 1$. Deep inelastic scatterings are characterised by a large momentum transfer q between the electron and the proton: $Q^2 \gg M^2$, $\nu \gg M$. The cross-section for deep inelastic scattering is usually defined in terms of the Lorentz invariant variables Q^2 and the Bjorken variable x , defined as $x = \frac{Q^2}{2P \cdot q}$, and are given by:

$$\frac{d^2\sigma}{dx dQ^2} = \frac{4\pi\alpha^2}{xQ^4} [(1-y)F_2(x, Q^2) - xy^2F_1(x, Q^2)] \quad ,$$

where $y = Q^2/(sx)$, $s = (P + p_e)^2$ is the centre-of-mass energy of the e-p system. The structure functions $F_1(x, Q^2)$ and $F_2(x, Q^2)$ are an extension of the form-factors for elastic scattering. The first measurements of high energy inclusive inelastic scattering experiments were carried out with a 20 GeV linear accelerator at SLAC, and showed that the structure functions $F_1(x, Q^2)$ and $F_2(x, Q^2)$ were independent of Q^2 at fixed x in the studied $1 < Q^2 < 10 \text{ GeV}^2/c^2$ range. This was in contrast to what was found for the proton elastic form factors, where a decrease of two orders of magnitude was observed in the same Q^2 interval. The observed behaviour was predicted by Bjorken in 1968 for $Q^2 \rightarrow \infty$ [38], and is known as *Bjorken scaling*. A physical interpretation of the phenomena arrived just one year later, in 1969, with Feynman's parton model [39], which described the interaction in terms of an elastic scattering of the probe off a point-like constituent (parton) of the proton. This explains the scale-invariance property of the proton structure functions, since the scattering centres are structure-less. In this picture, the Bjorken variable x gains a new interpretation as the fraction of the proton momentum carried by the struck parton. The parton model also provided with a simple definition of the structure functions in terms of the parton distribution functions $f_a(x)$:

$$F_2(x, Q^2) = \sum_a e_a^2 x f_a(x) \quad ,$$

where the sum is over partons with electric charge e_a , and f_a are unknown, but universal functions for a given hadron, describing the probability of finding a parton of type a with a fraction x of the proton momentum.

To study the spin properties of the partons, the structure functions F_1 and F_2 were studied at different centre-of-mass energies. By investigating the relationship between the two structure functions, it was established that the partons have spin 1/2, as the Callan-Gross relation [40], which is true for point-like Dirac

particles, was found to be satisfied:

$$F_2(x, Q^2) = 2xF_1(x, Q^2) \quad .$$

In the next years, it became clear that there must be other constituents in the proton carrying momentum, but not electric charge nor weak charge, as the so-called momentum sum rule was not saturated by the measured PDFs in electron and neutrino scatterings. The missing momentum was attributed to the gluons, which were discovered in the 1970s and are the field quantum of the strong force.

Bjorken scaling violation

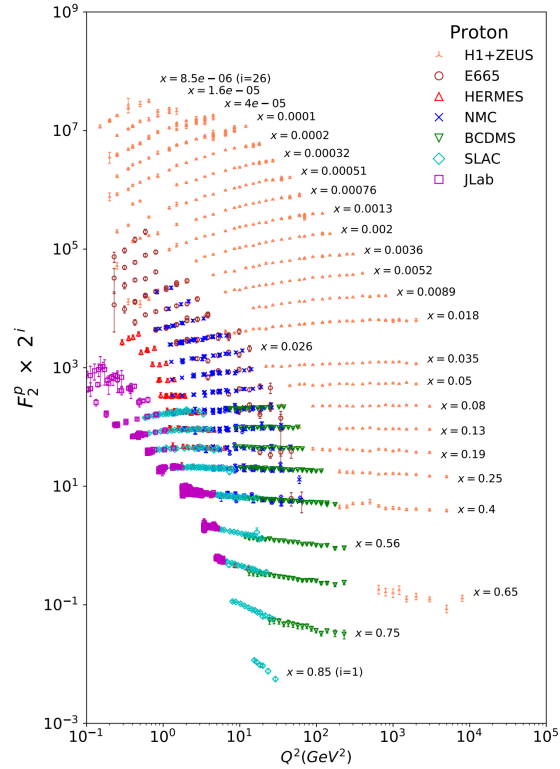


Figure 2.3: The proton structure function F_2^p measured in electromagnetic scattering of electrons and positrons on protons, and for electrons/positrons and muons on a fixed target [4].

By the end of the 1970s, measurements of the structure functions at larger Q^2 values taken at CERN and Desy showed that the Bjorken scaling was violated, i.e. the structure functions were not Q^2 independent. Figure 2.3 shows the measurements of proton structure functions $F_2(x, Q^2)$ as a function of Q^2 for

different values of x by different experiments [4]. It is clear from the plot that the structure functions present an increasing trend as a function of Q^2 at low x , and a decreasing trend as a function of Q^2 at high x . The parton model is not able to explain this behaviour as it relies on the assumption that the transferred energy is large enough to neglect the mass of the proton and its constituents, and the interactions between the partons. In particular, the partons' transverse momentum with respect to the proton momentum is neglected. The key point in understanding the Bjorken scaling violation comes from QCD and is that the parton's transverse momentum is not in fact restricted to be small. A quark can emit a gluon and acquire large transverse momentum k_T with a probability proportional to $\alpha_s dk_T/k_T^2$ at large k_T . The integral extends up to the kinematic limit $k_T \sim Q^2$, and gives rise to contributions proportional to $\alpha_s \log Q^2$, which break scaling.

Chapter 3

D^+ and D_s^+ reconstruction strategy in pp and Pb–Pb collisions

Due to their mean proper decay lengths ($c\tau$) of 151.2 μm and 309.8 μm respectively [4], D_s^+ and D^+ mesons and their charge conjugate cannot be directly detected by the ALICE detector, as they typically decay before reaching the detector. Consequently, their production is inferred through the reconstruction of their hadronic decays into $D_s^+(D^+) \rightarrow \phi\pi^+ \rightarrow K^+K^-\pi^+$ and their charge conjugates, with a branching ratio of 2.21×10^{-2} (2.69×10^{-3}). The spatial resolution capabilities of the ALICE detector ?? allow for the separation of the secondary decay vertices of D mesons from the primary interaction vertex, allowing to conduct an analysis based on the reconstruction and selection of secondary-vertex topologies characterised by relatively large separations from the primary interaction vertex. Furthermore, particle-identification (PID) information are exploited to improve the selection of the D mesons and their decay products and thus to reduce the background.

Two distinct categories of D mesons emerge based on their production mechanisms: *prompt* and *feed-down* D mesons. The former originate directly from the hadronisation of charm quarks or from the strong decay of excited open-charm or charmonium states. Conversely, feed-down D mesons are produced from the decay of hadrons containing a beauty quark. Decay vertices of feed-down D mesons are on average more displaced from the interaction vertex with respect to promptly-produced ones, due to the larger mean proper decay lengths of beauty hadrons ($c\tau \sim 500 \mu\text{m}$ [4]) as compared to charm hadrons. Therefore, exploiting the selection of displaced decay-vertex topologies, it is possible not only to separate D mesons from the combinatorial background, but also enables the discrimination between feed-down and prompt D mesons.

3.1 Data sample and event selection

The analyses reported in this Thesis are performed on a dataset of pp collisions at a centre-of-mass energy of $\sqrt{s} = 13.6$ TeV, collected by the ALICE detector during the 2022 data-taking period and on a dataset of Pb–Pb collision at a centre-of-mass energy per nucleon-nucleon collision of $\sqrt{s_{NN}} = 5.36$ TeV collected during 2023. **Aggiungere selezioni dei dati e fiducial acceptance!**

3.2 D_s^+ and D^+ decay-vertex reconstruction and selection

D_s^+ and D^+ mesons (and their charge conjugates) are reconstructed through their hadronic decay channel $D_s^+, D^+ \rightarrow \phi \pi^+ \rightarrow K^+ K^- \pi^+$. are constructed by combining triplets of tracks with the appropriate charge signs, i.e., (+, −, +) for D_s^+ and D^+ mesons, and (−, +, −) for their antiparticles. The decay vertex of the candidate is reconstructed through a minimisation of a χ^2 -like quantity, denoted as D :

$$D = \sqrt{\sum_{i=1}^3 \left[\left(\frac{x_i - x_0}{\sigma_{x_i}} \right)^2 + \left(\frac{y_i - y_0}{\sigma_{y_i}} \right)^2 + \left(\frac{z_i - z_0}{\sigma_{z_i}} \right)^2 \right]} \quad , \quad (3.1)$$

where (x_i, y_i, z_i) and $(\sigma_{x_i}, \sigma_{y_i}, \sigma_{z_i})$ represent the position and the uncertainty of the i -th track at the point of closest approach, respectively, while (x_0, y_0, z_0) denotes the position of the reconstructed vertex. The invariant mass and momentum of the D_s^+ and D^+ candidates are computed from the energy and momentum of the measured tracks evaluated at the point of closest approach to the decay vertex. The momentum of the candidate is defined as the sum of the momenta of the three track. For the invariant mass computation, the kaon mass is always assigned to the track with opposite charge sign with respect to the D-meson candidate (*opposite-sign track*). For the two *like-sign tracks*, the two pion-kaon mass hypothesis combinations (i.e. $(K^+ K^- \pi^+)$ and $(\pi^+ K^- K^+)$ for positively charged candidates) are considered.

A lot of triplets can be built from the tracks produced in a pp collision, and this number grows even more in a Pb–Pb collision, where the charged-particles multiplicity is much larger. Thus, many D_s^+ - and D^+ -meson candidates are created, the vast majority of them being combinatorial background. To increase the signal-over-background ratio and the statistical significance of the measurement, tight selections are required. The analyses presented in this Thesis exploit several selection criteria, which can be divided into:

- i Track-quality selections
- ii Selections based on the decay topology and kinematics
- iii Particle identification of the decay products

In the following, the applied selections are described in more details

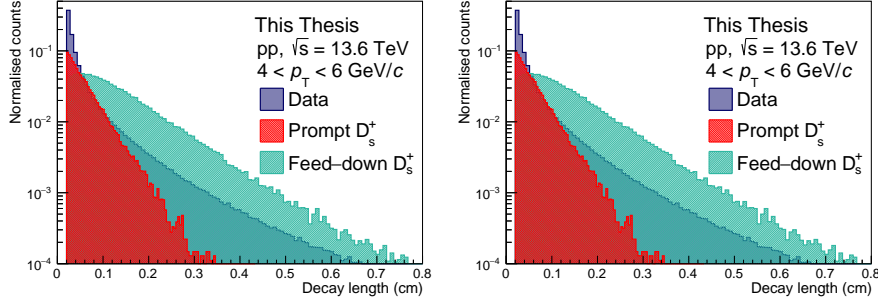


Figure 3.1: Caption

3.2.1 Track-quality selections

Only tracks that successfully pass strict quality and kinematic requirements are considered eligible for inclusion in the construction of D_s^+ - and D^+ -meson candidates. In particular, only ITS-TPC tracks with at least 70 (out of XX) associated space points in the TPC and are selected. [Aggiungere info ITS e selezioni di singola traccia](#)

3.2.2 Topological selections

D_s^+ and D^+ mesons exhibit a displaced decay vertex topology, which can be used to separate the signal from the uninteresting combinatorial background. Moreover, promptly produced D mesons exhibit different topological features compared to feed-down D mesons, enabling further discrimination between the two production mechanisms. This differentiation potentially offers insights into beauty-quark production through the measurement of open-charm states. These selections are tuned as a function of the p_T in order to increase the signal-over-background and the statistical significance of the measurement. The different topological selections are presented herein. The corresponding distributions of variables are shown for the signal, which is divided into prompt and feed-down contributions and obtained from Monte Carlo simulations, as well as the combinatorial background, which is obtained in a invariant-mass region away from the signal region, denoted as *sidebands*. [Rifare figure cambiando colori e usando le sidebands](#)

Decay Length

The decay length is defined as the distance between the primary and secondary vertices. For D_s^+ and D^+ mesons, the decay length provides an approximation of the actual decay length, as the particle's curvature resulting from the motion in the presence of a magnetic field is not considered. However, given the small mean proper decay length of $\sim 150(300) \mu\text{m}$ of the D_s^+ (D^+) mesons, this effect is negligible. This is one of the most important variables to distinguish between

the signal and the combinatorial background, since the displaced topology of the signal shifts the decay length distribution towards greater values. Furthermore, since beauty hadrons have a larger mean proper decay length than D_s^+ and D^+ mesons, the feed down decay length distribution is particularly shifted towards larger values, allowing for an easier separation of this production mechanism from the background. The distribution of the decay length also depends on the p_T of the D meson, because of the Lorentz boost which increases the travelled distance in the laboratory reference frame.

Bibliography

- [1] M. Gell-Mann, “A Schematic Model of Baryons and Mesons”, *Phys. Lett.* **8** (1964) 214–215.
- [2] G. Zweig, *An $SU(3)$ model for strong interaction symmetry and its breaking. Version 2*, pp. 22–101. 2, 1964.
- [3] H. Fritzsch and M. Gell-Mann, “Current algebra: Quarks and what else?”, *eConf C720906V2* (1972) 135–165, [arXiv:hep-ph/0208010](#).
- [4] **Particle Data Group** Collaboration, R. L. Workman and Others, “Review of Particle Physics”, *PTEP* **2022** (2022) 083C01.
- [5] F. Herzog, B. Ruijl, T. Ueda, J. A. M. Vermaseren, and A. Vogt, “The five-loop beta function of Yang-Mills theory with fermions”, *JHEP* **02** (2017) 090, [arXiv:1701.01404 \[hep-ph\]](#).
- [6] K. Johnson, “The M.I.T. Bag Model”, *Acta Phys. Polon. B* **6** (1975) 865.
- [7] R. P. Feynman, “Space-time approach to non-relativistic quantum mechanics”, *Rev. Mod. Phys.* **20** (Apr, 1948) 367–387.
<https://link.aps.org/doi/10.1103/RevModPhys.20.367>.
- [8] **BMW** Collaboration, S. Durr *et al.*, “Ab-Initio Determination of Light Hadron Masses”, *Science* **322** (2008) 1224–1227, [arXiv:0906.3599 \[hep-lat\]](#).
- [9] **HotQCD** Collaboration, A. Bazavov *et al.*, “Equation of state in (2+1)-flavor QCD”, *Phys. Rev. D* **90** (2014) 094503, [arXiv:1407.6387 \[hep-lat\]](#).
- [10] S. Borsanyi, Z. Fodor, C. Hoelbling, S. D. Katz, S. Krieg, and K. K. Szabo, “Full result for the QCD equation of state with 2+1 flavors”, *Phys. Lett. B* **730** (2014) 99–104, [arXiv:1309.5258 \[hep-lat\]](#).
- [11] **ALICE** Collaboration, “The ALICE experiment – A journey through QCD”, [arXiv:2211.04384 \[nucl-ex\]](#).

- [12] **NA38, NA50** Collaboration, M. C. Abreu *et al.*, “Dimuon and charm production in nucleus-nucleus collisions at the CERN SPS”, *Eur. Phys. J. C* **14** (2000) 443–455.
- [13] **NA50** Collaboration, M. C. Abreu *et al.*, “Anomalous J / ψ suppression in Pb - Pb interactions at 158 GeV/c per nucleon”, *Phys. Lett. B* **410** (1997) 337–343.
- [14] R. Nouicer, “Formation of Dense Partonic Matter in High Energy Heavy-Ion Collisions: Highlights of RHIC Results”, in *Advanced Studies Institute on Symmetries and Spin (SPIN-Praha-2008)*. 1, 2009. [arXiv:0901.0910 \[nucl-ex\]](#).
- [15] **ALICE** Collaboration, C. Loizides, “Charged-particle multiplicity and transverse energy in Pb-Pb collisions at $\sqrt{s_{NN}} = 2.76$ TeV with ALICE”, *J. Phys. G* **38** (2011) 124040, [arXiv:1106.6324 \[nucl-ex\]](#).
- [16] J. D. Bjorken, “Highly Relativistic Nucleus-Nucleus Collisions: The Central Rapidity Region”, *Phys. Rev. D* **27** (1983) 140–151.
- [17] **PHENIX** Collaboration, K. Adcox *et al.*, “Formation of dense partonic matter in relativistic nucleus-nucleus collisions at RHIC: Experimental evaluation by the PHENIX collaboration”, *Nucl. Phys. A* **757** (2005) 184–283, [arXiv:nucl-ex/0410003](#).
- [18] A. Andronic, P. Braun-Munzinger, K. Redlich, and J. Stachel, “Decoding the phase structure of QCD via particle production at high energy”, *Nature* **561** (2018) 321–330, [arXiv:1710.09425 \[nucl-th\]](#).
- [19] E. Schnedermann, J. Sollfrank, and U. W. Heinz, “Thermal phenomenology of hadrons from 200-A/GeV S+S collisions”, *Phys. Rev. C* **48** (1993) 2462–2475, [arXiv:nucl-th/9307020](#).
- [20] F. Cooper and G. Frye, “Comment on the Single Particle Distribution in the Hydrodynamic and Statistical Thermodynamic Models of Multiparticle Production”, *Phys. Rev. D* **10** (1974) 186.
- [21] M. L. Miller, K. Reygers, S. J. Sanders, and P. Steinberg, “Glauber modeling in high energy nuclear collisions”, *Ann. Rev. Nucl. Part. Sci.* **57** (2007) 205–243, [arXiv:nucl-ex/0701025](#).
- [22] M. Bleicher *et al.*, “Relativistic hadron hadron collisions in the ultrarelativistic quantum molecular dynamics model”, *J. Phys. G* **25** (1999) 1859–1896, [arXiv:hep-ph/9909407](#).
- [23] Z.-W. Lin, C. M. Ko, B.-A. Li, B. Zhang, and S. Pal, “A Multi-phase transport model for relativistic heavy ion collisions”, *Phys. Rev. C* **72** (2005) 064901, [arXiv:nucl-th/0411110](#).

- [24] **ALICE** Collaboration, S. Acharya *et al.*, “Transverse momentum spectra and nuclear modification factors of charged particles in pp, p-Pb and Pb-Pb collisions at the LHC”, *JHEP* **11** (2018) 013, [arXiv:1802.09145 \[nucl-ex\]](#).
- [25] B. Z. Kopeliovich, J. Nemchik, A. Schafer, and A. V. Tarasov, “Cronin effect in hadron production off nuclei”, *Phys. Rev. Lett.* **88** (2002) 232303, [arXiv:hep-ph/0201010](#).
- [26] R. Baier, Y. L. Dokshitzer, A. H. Mueller, S. Peigne, and D. Schiff, “Radiative energy loss of high-energy quarks and gluons in a finite volume quark - gluon plasma”, *Nucl. Phys. B* **483** (1997) 291–320, [arXiv:hep-ph/9607355](#).
- [27] J. Rafelski and B. Muller, “Strangeness Production in the Quark - Gluon Plasma”, *Phys. Rev. Lett.* **48** (1982) 1066. [Erratum: *Phys.Rev.Lett.* 56, 2334 (1986)].
- [28] **STAR** Collaboration, B. I. Abelev *et al.*, “Enhanced strange baryon production in Au + Au collisions compared to p + p at $s(NN)^{1/2} = 200$ -GeV”, *Phys. Rev. C* **77** (2008) 044908, [arXiv:0705.2511 \[nucl-ex\]](#).
- [29] **ALICE** Collaboration, B. B. Abelev *et al.*, “Multi-strange baryon production at mid-rapidity in Pb-Pb collisions at $\sqrt{s_{NN}} = 2.76$ TeV”, *Phys. Lett. B* **728** (2014) 216–227, [arXiv:1307.5543 \[nucl-ex\]](#). [Erratum: *Phys.Lett.B* 734, 409–410 (2014)].
- [30] **ALICE** Collaboration, J. Adam *et al.*, “Enhanced production of multi-strange hadrons in high-multiplicity proton-proton collisions”, *Nature Phys.* **13** (2017) 535–539, [arXiv:1606.07424 \[nucl-ex\]](#).
- [31] **ALICE** Collaboration, B. B. Abelev *et al.*, “Multiplicity Dependence of Pion, Kaon, Proton and Lambda Production in p-Pb Collisions at $\sqrt{s_{NN}} = 5.02$ TeV”, *Phys. Lett. B* **728** (2014) 25–38, [arXiv:1307.6796 \[nucl-ex\]](#).
- [32] **ALICE** Collaboration, J. Adam *et al.*, “Multi-strange baryon production in p-Pb collisions at $\sqrt{s_{NN}} = 5.02$ TeV”, *Phys. Lett. B* **758** (2016) 389–401, [arXiv:1512.07227 \[nucl-ex\]](#).
- [33] J. C. Collins, D. E. Soper, and G. F. Sterman, “Factorization of Hard Processes in QCD”, *Adv. Ser. Direct. High Energy Phys.* **5** (1989) 1–91, [arXiv:hep-ph/0409313](#).
- [34] **ALICE** Collaboration, S. Acharya *et al.*, “Measurement of beauty and charm production in pp collisions at $\sqrt{s} = 5.02$ TeV via non-prompt and prompt D mesons”, *JHEP* **05** (2021) 220, [arXiv:2102.13601 \[nucl-ex\]](#).
- [35] M. Cacciari, S. Frixione, and P. Nason, “The p(T) spectrum in heavy flavor photoproduction”, *JHEP* **03** (2001) 006, [arXiv:hep-ph/0102134](#).

- [36] T. Sjöstrand, S. Ask, J. R. Christiansen, R. Corke, N. Desai, P. Ilten, S. Mrenna, S. Prestel, C. O. Rasmussen, and P. Z. Skands, “An introduction to PYTHIA 8.2”, *Comput. Phys. Commun.* **191** (2015) 159–177, [arXiv:1410.3012 \[hep-ph\]](#).
- [37] J. I. Friedman and H. W. Kendall, “Deep inelastic electron scattering”, *Ann. Rev. Nucl. Part. Sci.* **22** (1972) 203–254.
- [38] J. D. Bjorken, “Asymptotic Sum Rules at Infinite Momentum”, *Phys. Rev.* **179** (1969) 1547–1553.
- [39] R. P. Feynman, “Very high-energy collisions of hadrons”, *Phys. Rev. Lett.* **23** (1969) 1415–1417.
- [40] C. G. Callan, Jr. and D. J. Gross, “High-energy electroproduction and the constitution of the electric current”, *Phys. Rev. Lett.* **22** (1969) 156–159.